

## Disentangling nanoscale electric and magnetic fields by time-reversal operation in differential phase-contrast STEM.

M. Campanini,<sup>1\*</sup> L. Nasi,<sup>2</sup> F. Albertini<sup>2</sup>, R. Erni<sup>1</sup>

### AFFILIATIONS

<sup>1</sup>*Electron Microscopy Center, Empa – Swiss Federal Laboratories for Materials Science and Technology, Ueberlandstrasse 129, 8600 Duebendorf, Switzerland*

<sup>2</sup>*Istituto dei Materiali per l'Elettronica ed il Magnetismo, IMEM-CNR, Parco delle Scienze 37/A, 43124 Parma, Italy*

\*Author to whom correspondence should be addressed: marco.campanini@empa.ch

---

### ABSTRACT

Differential phase-contrast (DPC) scanning transmission electron microscopy (STEM) has recently attracted significant interest for allowing mapping electrostatic and magnetic fields at high-spatial-resolution. Nevertheless, due to its simultaneous sensitivity to both electrostatic and magnetic fields, the interpretation of DPC measurements on magnetic specimens is not straightforward. In this work, we demonstrate that the two contributions to the Lorentz force can be separated by means of the time-reversal operation of the electron beam. In practice, such a condition is easily achieved by repeating the DPC-STEM measurement after flipping the specimen by 180° degrees. The separation of the two contributions allows discriminating the effects of the electrostatic potential, like e.g. the thickness variation in a specimen with uniform composition, from the actual magnetic signal. This finding opens a new perspective in the nanoscale study of magnetic nanostructure by DPC-STEM or, more generally, by 4D-STEM.

---

The entanglement between electrostatic and magnetic fields plays a fundamental role in materials science, being the source of a rich phenomenology that spans from multiferroism to superconductivity.<sup>1,2</sup> On the other hand, the experimental discrimination between local electrostatic and magnetic fields is a challenging problem that hampers the full comprehension of the behavior of various physical systems.

One of the most striking difficulties in the investigation of the electromagnetic properties of functional materials is represented, in fact, by the simultaneous measurement of their internal electric and magnetic field with nanoscale resolution. In this regard, an electron beam constitutes an effective probe with the key advantages that (i) the electrons can be focused in a small probe (whose diameter can be equal or smaller than one nanometer) and (ii) they are charged particles interacting with the electromagnetic fields, thanks to the Lorentz force.

The sensitivity of an electron beam to either electric or magnetic fields has been recently demonstrated.<sup>3–7</sup> For example, a focused electron probe was successfully employed to study the internal electric field in a p-n junction by differential phase-contrast (DPC) scanning transmission electron microscopy (STEM).<sup>8,9</sup> Similarly, the nanoscale magnetic domain configuration can be mapped by measuring the Lorentz deflection of the beam due to the specimen magnetization.<sup>5,10–15</sup>

In this Letter, we demonstrate that Lorentz field mapping – performed by applying the time-reversal operation of the electron beam – in DPC-STEM allows for simultaneous mapping of the electric and magnetic fields with nanometer resolution and for efficiently disentangling their contributions.

The study was performed on a system composed of free-standing Ni<sub>2</sub>MnGa disks with a sub-micrometer lateral size. The disks were obtained by lithographic patterning of continuous thin films and their shape is a truncated cone.<sup>16</sup> Fig. 1a shows an annular dark-field (ADF) image of a cluster of 7 disks deposited on a carbon/holey TEM grid. The disks shape geometry – with a finite difference between the top and bottom surfaces of the truncated cone – is responsible for a variation of the contrast in the outer area of the disk, as highlighted by the line profile taken along the white dashed line in Fig. 1a. In particular, this contrast change in the ADF signal arises because of the thickness variation at the edges of the disks.

We then performed DPC-STEM experiments, as schematized in Fig. 1b. Both the ADF and DPC signals were recorded in Lorentz mode, i.e. switching the magnetic field of the objective lens off to ensure that the sample is in a field-free environment. In Lorentz STEM mode, the beam convergence angle is reduced to 0.20 mrad. Although this electron-optical configuration delivers a resolution limited to about a nanometer, it assures a higher field sensitivity.<sup>17</sup> In particular, the beam deflection due to the Lorentz force is efficiently detected by measuring the differential signal between opposite quadrants of a segmented annular detector. More details about the experimental settings are available in S1 of Supplementary Information.

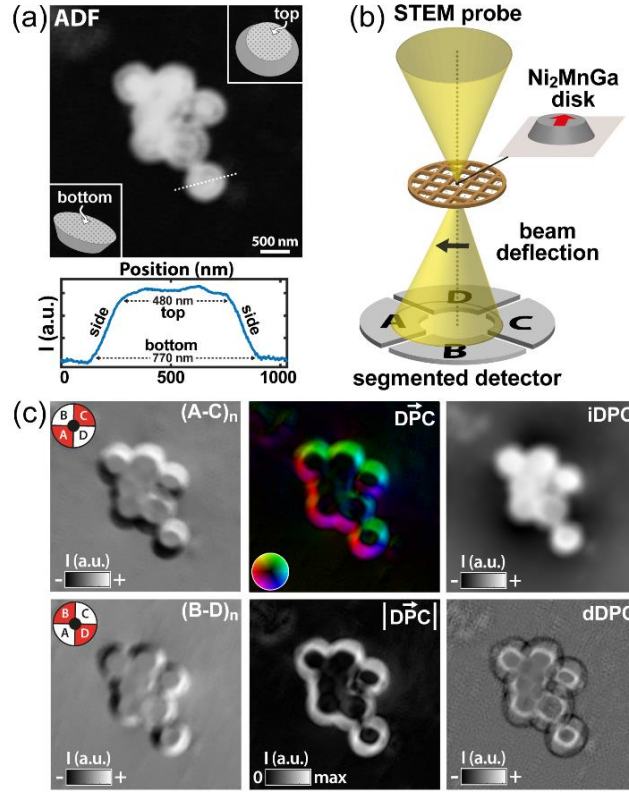


Fig. 1 (a) Annular dark-field image of  $\text{Ni}_2\text{MnGa}$  disks suspended on a carbon-coated TEM grid. The shape of the disks corresponds to a truncated cone, as highlighted by the intensity line-profile. (b) Schematic representation of the DPC-STEM measurement, depicting the Lorentz deflection due to a nanoscale magnetic field. (c) DPC-STEM measurement showing the effects of the shape-induced non-uniform thickness.

Fig. 1c shows the DPC signals obtained in the same area as in Fig 1a. In particular, the  $(A-C)_n$  and  $(B-D)_n$  signals were obtained by normalizing the differential signals to the total intensity detected by the annular segmented detector,<sup>18</sup> to correct absorption and/or diffraction effects that may induce a change in the diffraction pattern's intensity (see S2 in Supplementary Information for more details).

A remarkable variation in the differential  $(A-C)_n$  and  $(B-D)_n$  signals is observed at the edges of the disks, which corresponds to a field distribution strongly related to the specimen thickness gradient. This result can be straightforwardly understood with basic consideration about the sample geometry (Fig. S3, Supplementary Information). Accordingly, also the phase and charge density (given by the integrated-DPC and differential-DPC signals, respectively named iDPC and dDPC) are strongly affected by the specimen's thickness variation. Therefore, due to the non-uniform specimen thickness, no information about the magnetic configuration of the specimen can be directly extracted by a single DPC-STEM measurement. On the contrary, the local thickness variations due to the specimen geometry – particularly important for various magnetic nanostructures with different shapes – can lead to misinterpretation of the experimental results.

The investigation of the magnetic properties of a specimen using an electron probe thus strongly relies on the capability of separating the two contributions to the Lorentz force. Here, we propose an approach based on the time-reversal operation of the electron beam, previously proposed for electron holography.<sup>19</sup> In particular, since the beam deflection due to the magnetic component of the Lorentz force changes its sign under the time-reversal operation, we can combine two DPC-STEM measurements to disentangle the electrostatic and magnetic fields in the specimen. Fig. 2a and b depict this scenario, where the time-reversal condition is more conveniently achieved by rotating the specimen upside-down rather than changing the direction of the beam propagation. By performing the sum and the difference of the detected differential contrast, the electrostatic and magnetic fields can be separated (Fig. 2c).

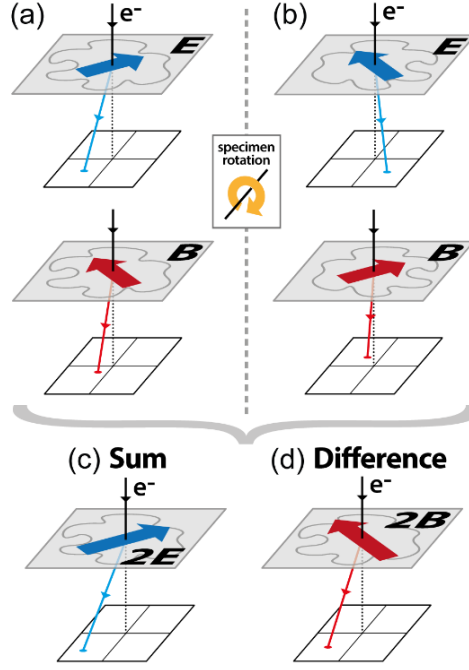


Fig. 2 Lorentz deflections of the electron beam due to the electrostatic and magnetic fields in the specimen (a) before and (b) after flipping the specimen by  $180^\circ$ . The (c) electrostatic and (d) magnetic components of the Lorentz force are computed by performing respectively the sum and the subtraction of the DPC-STEM images.

We thus applied this separation methodology to the described case study. To perform the separation procedure, a second DPC-STEM experiment was performed after flipping upside-down the specimen (i.e.  $180^\circ$  rotation) and keeping all the experimental conditions invariant. It is worth noting that despite a careful execution of the flipping procedure, we unavoidably introduce a small deviation of the in-plane specimen rotation with respect to the segmented ADF quadrants, i.e. the main axes of the DPC vector components obtained after flipping the specimen are slightly rotated with respect to the ones of the direct experiments. Therefore, the DPC-STEM signals generated after flipping the specimen need to be properly aligned and re-calculated along the main directions of the direct experiment (Fig. S4, Supplementary Information). To minimize the image distortions, the signal alignment was performed using the *BigWarp* tool for Fiji,<sup>20</sup> which allows an interactive landmark-based deformable image alignment.

The separation approach allows thus to calculate the electrostatic and magnetic contributions to the DPC-STEM signal and similarly, can be applied to the iDPC and dDPC signals to obtained respectively the two contributions to the phase (i.e. projected electrostatic potential and magnetic vector potential) and the equivalent projected density of electrical charges and Amperian current density.

The results of the separation are shown in Fig. 3. Figs. 3a and b show, respectively, the phase contours of the electrostatic and magnetic phase shifts plotted superimposed to the electrostatic phase shift. In particular, the phase contours of the electrostatic phase shift correspond to the electric field equipotential lines, while the phase contours of the magnetic phase shift represent the magnetic induction flux lines. A plot of the electric and magnetic phase shifts used for the calculation of the corresponding phase contours is given in Fig. S5 of Supplementary Information.

As visible from Fig. 3a, the phase contours of the electrostatic phase shift are localized at the edges of the disks. In the absence of an applied external electric field and for a sample with uniform composition, the only variation of the electrostatic phase shift is associated with the change of the specimen's thickness. On the contrary, the magnetic flux lines are not solely localized at the edges of the disks (Fig. 3b). Since the specimen is the same studied in Ref. 16, both regions with in-plane and out-of-plane magnetization are expected in the free-standing martensitic disks that have undergone a thermal cycle.

Fig. 3c and e show respectively the projected electric field, and the projected charge density. The field of view of Fig. 3a was chosen larger compared to the one of b and c to highlight that no other significant variation of the projected electrostatic potential is observed far from the  $\text{Ni}_2\text{MnGa}$  truncated cones. As previously mentioned, (see Fig. S3 in Supplementary Information), the variation of local thickness due to the specimen shape is responsible for the local electric field at the edges of the disks (Fig. 3c) and for the corresponding projected electric charges (Fig. 3e).

Analogously, Figs. 3d and f show respectively the projected in-plane magnetic field and the corresponding equivalent Amperian current density. The magnetic induction map shows that areas with local in-plane

magnetization exist within the  $\text{Ni}_2\text{MnGa}$  disks and are preferentially located at the edges of the truncated cones, as a flux-closure geometry of the magnetic structure is achieved in free-standing disks (in agreement with the observation of Ref. [16]). Therefore, the proposed methodology permits to measure the electrostatic and magnetic fields at the nanoscale by DPC-STEM technique. Our results represent a proof-of-concept experiment of the applicability of the time-reversal operation of the electron beam in DPC-STEM.

These findings highlight the importance of separating the two contributions of the Lorentz force on the deflection of the electron beam, as it occurs in DPC-STEM experiments on magnetic materials. In addition to the fundamental interest in the discrimination of entangled electrostatic and magnetic fields, the proposed separation approach opens new possibilities in the study of nanostructured magnetic materials by DPC-STEM and, more generally, four-dimensional (4D) STEM.

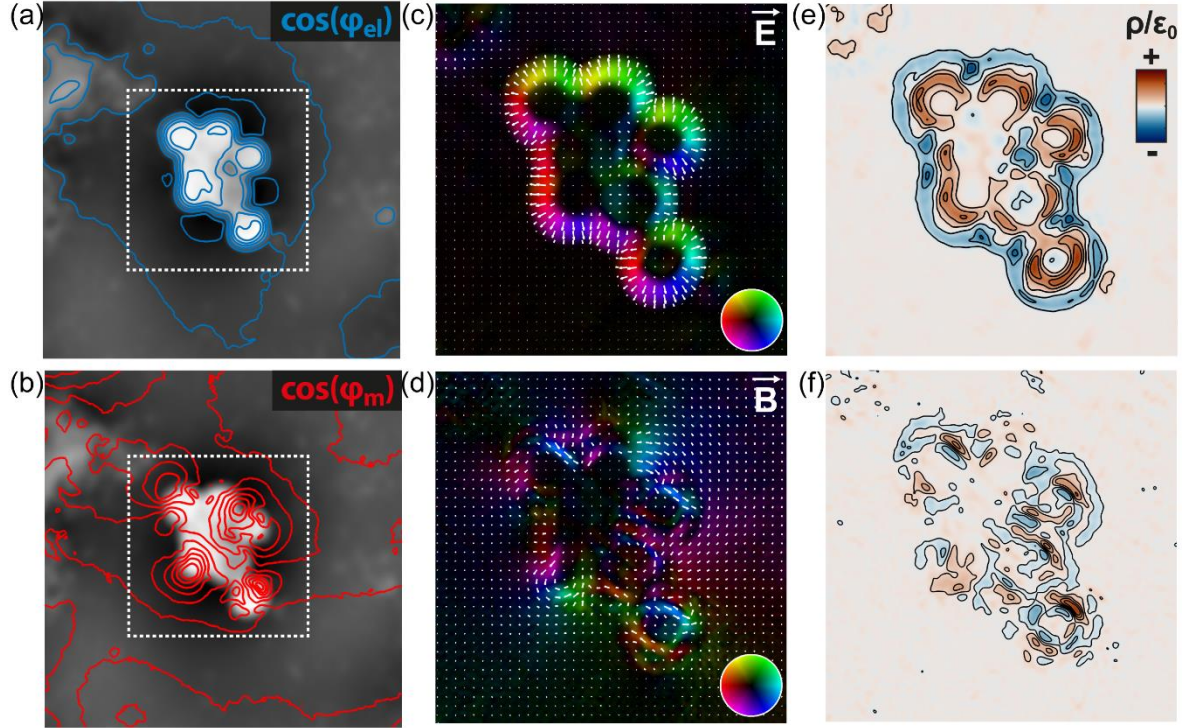


Fig. 3 Phase contours of the (a) electrostatic and (b) magnetic phase shifts obtained by the separation approach. The phase contours are shown overlaid on the electrostatic phase shift. (c) Electrostatic field and (d) magnetic induction vector maps. (e) Projected electrical charges and (f) projected Amperian current density. The field of view of (c-f) corresponds to the dashed areas in (a) and (b).

## ACKNOWLEDGMENTS

M.C. and R.E acknowledge financial support by the InnoSuisse Project N. 35839.1 IP-ENG and by the European Research Council (ERC) under the EU's Horizon 2020 research and innovation program (grant No. 681312). The authors gratefully acknowledge Paola Tiberto and Federica Celegato for the lithographic patterning of the  $\text{Ni}_2\text{MnGa}$  thin films.

## DATA AVAILABILITY

The data that support the findings of this study are available from the corresponding author upon reasonable request.

## REFERENCES

- <sup>1</sup> M. Fiebig, T. Lottermoser, D. Meier, and M. Trassin, *Nat. Rev. Mater.* **1**, 16046 (2016).
- <sup>2</sup> K. Ueno, S. Nakamura, H. Shimotani, A. Ohtomo, N. Kimura, T. Nojima, H. Aoki, Y. Iwasa, and M. Kawasaki, *Nat. Mater.* **7**, 855 (2008).
- <sup>3</sup> N. Shibata, S.D. Findlay, Y. Kohno, H. Sawada, Y. Kondo, and Y. Ikuhara, *Nat. Phys.* **8**, 611 (2012).
- <sup>4</sup> M. Campanini, R. Erni, C.H. Yang, R. Ramesh, and M.D. Rossell, *Nano Lett.* **18**, 717 (2018).
- <sup>5</sup> T. Matsumoto, Y.-G. So, Y. Kohno, H. Sawada, Y. Ikuhara, and N. Shibata, *Sci. Adv.* **2**, (2016).
- <sup>6</sup> R. Article, *J. Phys. D. Appl. Phys.* **17**, 1 (2001).
- <sup>7</sup> J.A. Hachtel, J.C. Idrobo, and M. Chi, *Adv. Struct. Chem. Imaging* **4**, 10 (2018).
- <sup>8</sup> N. Shibata, S.D. Findlay, H. Sasaki, T. Matsumoto, H. Sawada, Y. Kohno, S. Otomo, R. Minato, and Y. Ikuhara, *Sci. Rep.* **5**, 10040 (2015).
- <sup>9</sup> S. Toyama, T. Seki, S. Anada, H. Sasaki, K. Yamamoto, Y. Ikuhara, and N. Shibata, *Ultramicroscopy* **216**, 113033 (2020).
- <sup>10</sup> T. Sannomiya, Y. Haga, Y. Nakamura, O. Nittono, and Y. Takahashi, *J. Appl. Phys.* **95**, 214 (2004).
- <sup>11</sup> T. Matsumoto, Y.G. So, Y. Kohno, Y. Ikuhara, and N. Shibata, *Nano Lett.* **18**, 754 (2018).
- <sup>12</sup> M. Krajnak, D. McGrouther, D. Maneuski, V. O'Shea, and S. McVitie, *Ultramicroscopy* **165**, 42 (2016).
- <sup>13</sup> S. McVitie and J.N. Chapman, *J. Magn. Magn. Mater.* **83**, 97 (1990).
- <sup>14</sup> T. Sekiguchi, D. Watanabe, and K. Tsuno, *Jpn. J. Appl. Phys.* **24**, 1229 (1985).
- <sup>15</sup> Y.O. Murakami, T. Seki, A. Kinoshita, T. Shoji, Y. Ikuhara, and N. Shibata, *Microscopy* (2020).
- <sup>16</sup> M. Campanini, L. Nasi, S. Fabbrici, F. Casoli, F. Celegato, G. Barrera, V. Chiesi, E. Bedogni, C. Magén, V. Grillo, G. Bertoni, L. Righi, P. Tiberto, and F. Albertini, *Small* **14**, 1803027 (2018).
- <sup>17</sup> B. Haas, J.-L. Rouvière, V. Boureau, R. Berthier, and D. Cooper, *Ultramicroscopy* (2018).
- <sup>18</sup> F. Schwarzhuber, P. Melzl, and J. Zweck, *Ultramicroscopy* **177**, 97 (2017).
- <sup>19</sup> A. Tonomura, T. Matsuda, J. Endo, T. Arii, and K. Mihama, *Phys. Rev. B* **34**, 3397 (1986).
- <sup>20</sup> J.A. Bogovic, P. Hanslovsky, A. Wong, and S. Saalfeld, in *Proc. - Int. Symp. Biomed. Imaging* (IEEE Computer Society, 2016), pp. 1123–1126.